Contents lists available at ScienceDirect

Icarus

journal homepage: www.elsevier.com/locate/icarus

Lunar cold spots: Granular flow features and extensive insulating materials surrounding young craters

Joshua L. Bandfield [a,*], Eugenie Song [b], Paul O. Hayne [c], Brittany D. Brand [d], Rebecca R. Ghent [e], Ashwin R. Vasavada [c], David A. Paige [f]

[a] Space Science Institute, USA
[b] Hawai'i Institute of Geophysics and Planetology, University of Hawai'i, USA
[c] Jet Propulsion Laboratory, California Institute of Technology, USA
[d] Department of Geosciences, Boise State University, USA
[e] Department of Geology, University of Toronto, Canada
[f] Earth and Space Sciences, UCLA, USA

ARTICLE INFO

Article history:
Received 21 August 2013
Revised 14 December 2013
Accepted 17 December 2013
Available online xxxx

Keywords:
Moon, surface
Impact processes
Infrared observations
Regoliths

ABSTRACT

Systematic temperature mapping and high resolution images reveal a previously unrecognized class of small, fresh lunar craters. These craters are distinguished by near-crater deposits with evidence for lateral, ground-hugging transport. More distal, highly insulating surfaces surround these craters and do not show evidence of either significant deposition of new material or erosion of the substrate. The near-crater deposits can be explained by a laterally propagating granular flow created by impact in the lunar vacuum environment. Further from the source crater, at distances of ~10–100 crater radii, the upper few to 10s of centimeters of regolith appear to have been "fluffed-up" without the accumulation of significant ejecta material. These properties appear to be common to all impacts, but quickly degrade in the lunar space weathering environment. Cratering in the vacuum environment involves a previously unrecognized set of processes that leave prominent, but ephemeral, features on the lunar surface.

1. Introduction

Impact cratering is the dominant geologic process currently shaping the lunar surface. Both large and small scale impacts leave their imprint on the surface morphology and materials. Any observations from orbit or the surface must be viewed through the lens of impact cratering and take into account the physical and chemical changes caused by impact events. Terrestrial and laboratory studies have provided us with much of what we know about impact processes (e.g., Braslau, 1970; Melosh, 1989; Osinski et al., 2011; Housen and Holsapple, 2011). However, the extreme velocities and energies involved make it difficult to recreate impact conditions in the laboratory, especially at larger scales in a vacuum (Braslau, 1970; Housen and Holsapple, 2011). In addition, impact craters accessible for study on Earth are quickly degraded and modified, erasing many of the finer scale and more delicate properties that could reveal details about the conditions present at the time of impact (e.g., Osinski et al., 2011). These properties include loose, fine particulates and thin, discontinuous surface modifications at large distances from the impact site.

In situ and orbital studies of the lunar surface itself present an opportunity to characterize the details of well preserved impact craters. The recent resurgence in lunar observations from orbiting spacecraft such as Kaguya, Chang'e 1 and 2, Chandrayaan-1, and the Lunar Reconnaissance Orbiter (LRO) has provided a series of systematic, high quality observations showing details that have given rise to new perspectives on the development of the Moon. These new observations build on decades of lunar cratering studies based on the wealth of information returned from the Apollo and Luna programs of the 1960s and 1970s (e.g., Heiken et al., 1991).

In particular, thermal infrared mapping of the lunar surface can be used to determine near-surface thermophysical and compositional properties. Initial telescopic and Apollo 17 Infrared Scanning radiometer measurements were used to show that most lunar surfaces are covered by a fine particulate regolith (Shorthill, 1970; Mendell and Low, 1974). Isolated surfaces with warm nighttime temperatures were identified as rocky ejecta from relatively young craters that had not yet degraded in the lunar space weathering environment (Mendell and Low, 1974).

More recently, the Diviner Lunar Radiometer Experiment aboard the LRO spacecraft has acquired systematic global diurnal temperature measurements (Paige et al., 2010). These data have been used to characterize the near surface thermophysical environment, including polar temperatures, global rock abundances,

* Corresponding author. Address: Space Science Institute, 4750 Walnut Street, Suite 205, Boulder, CO 80301, USA.
E-mail address: jbandfield@spacescience.org (J.L. Bandfield).

http://dx.doi.org/10.1016/j.icarus.2013.12.017

and typical lunar regolith fines layering and thermophysical properties (e.g., Paige et al., 2010; Bandfield et al., 2011; Vasavada et al., 2012). These and other studies have revealed that lunar surface temperatures are highly sensitive to properties such as density and particle size distribution of the upper 10s of cm of the lunar regolith. These properties are a result of a delicate balance of impact and other processes that produce a highly structured regolith over time (e.g., Keihm and Langseth, 1973; Vasavada et al., 2012; Hayne et al., 2011; Ghent et al., 2012). For example, seismic events and overburden act to compress and increase the bulk density of the regolith, while micrometeorite impacts have a tendency to disrupt the regolith, lowering its bulk density. Even slight changes in the packing or rock concentration cause a temperature contrast relative to typical lunar regolith that can be readily detected in Diviner temperature measurements (e.g., Vasavada et al., 2012; Hayne et al., 2011; Bandfield et al., 2012).

In addition, recent high-resolution images returned from the LRO Camera (LROC; Robinson et al., 2010) have allowed for the characterization of lunar surface textures and morphology at meter scales. These images show detailed properties of recent impact craters at a finer scale than previously possible (e.g., Stopar et al., 2010). Because most impacts are small and their fine-scale features are quickly degraded, these new high resolution images of recent impact craters can show properties that provide new clues to details of impact processes.

The systematic temperature mapping by Diviner and high resolution images from LROC reveal a previously unrecognized class of small, fresh lunar craters with unique thermophysical and morphological properties. These craters are distinguished by near-crater deposits with evidence for lateral, ground-hugging transport. More distal, highly insulating surfaces surround these craters and do not show evidence of either significant deposition of new material or erosion of the pre-existing substrate. The near-crater deposits can be explained by a laterally propagating granular flow created by impact in the lunar vacuum environment. Further from the source crater, at distances of ~10–100 crater radii, regolith surfaces appear to have been "fluffed-up" without the accumulation of significant ejecta material. These properties appear to be common to all recent impacts, but quickly degrade in the lunar space weathering environment.

2. Data and methods

2.1. Instrument description and data

The Diviner Radiometer has 7 thermal infrared spectral channels; 3 spectral filters are near 8 μm wavelengths and separate filters cover ~13–23, 25–41, 50–100, and 100–400 μm wavelengths (Paige et al., 2010). Each channel consists of a 1 by 21 element detector array and separate spectral channels are arranged and data are collected in a pushbroom configuration. The spatial sampling of Diviner is ~160 by 320 m from a 50 km polar orbit and the local time of observations migrated across the full diurnal cycle throughout the primary LRO mission. More complete descriptions of the Diviner instrument characteristics and operations are given in Paige et al. (2010).

The data used for the analysis of individual craters were derived from the level 2 gridded data products available at the Planetary Data System (Paige et al., 2011). These data are constructed from the individual Diviner RDR measurements and resampled to 128 pixels per degree (ppd). We used data collected from Diviner channels 6–8 (with full width half maximum bandpasses of 13–23, 25–41, and 50–100 μm respectively) acquired between July 5, 2009 and September 2, 2012 as well as gridded maps of the local time of each observation. Each of the maps covers a single lunar cycle (~28 days) resulting in 46 separate maps. Each pixel of each map essentially corresponds to a single location and acquisition time though it may represent an areally weighted average of measurements acquired by several detectors.

These data were used to derive rock abundance and rock-free regolith temperatures using the methods described in Bandfield et al. (2011). Briefly, rock temperatures are modeled a priori using the properties for vesicular basalt described by Horai and Simmons (1972) and the 1-dimensional thermal model described by Vasavada et al. (1999). Diviner channel 6–8 radiances are then fit using a non-linear least-squares algorithm with rock fraction and rock-free regolith temperature as free parameters used for the optimization. Data were restricted to local times of 1930 to 0530 to avoid anisothermality effects due to solar heating and shading on sub-pixel local slopes.

2.2. Cold spot identification and diurnal temperatures

The rock-free regolith temperature maps show thermophysically distinct surfaces that we have termed "cold spots" due to their cold nighttime surface temperatures relative to the surrounding terrain. The thermophysical properties of the lunar surface are remarkably uniform and the cold spots are one of the few distinctive surface types. By comparison, the lunar highlands and maria are indistinguishable in night-time temperatures (Vasavada et al., 2012). Cold spots were initially identified by visual inspection of the temperature maps and cataloged using the global 128 ppd rock-free regolith temperature maps (Bandfield et al., 2011). Identifications were limited to surfaces equator-ward of 50°N/S. The number of cold spots that were identified is likely an underestimate due to residual temperature variations present on sloped surfaces, especially at high latitudes and in rough highlands terrain. These surfaces have significant temperature variations on slopes due to variable solar heating that persists through the lunar night. The variable surface temperatures interfere with the identification of cold spots to such a degree that they could not be distinguished and positively identified at latitudes greater than ~50°N/S. The variability of the surrounding terrain prevents a simple identification of cold spots based on quantitative parameters, such as temperature. The criteria for the positive identification of a cold spot is the presence of a coherent pattern of colder temperatures immediately surrounding a fresh crater (identified in the LROC Wide Angle Camera mosaic; Boyd et al., 2012) with no apparent topographic features that could be responsible for the cold temperatures.

We have identified 2060 individual cold spots between 50°S and 50°N using the 128 ppd Diviner night-time rock-free regolith temperature maps (Fig. 1). Cold spots show no obvious distribution pattern and appear randomly distributed, however a test for spatial randomness within 20 degrees of the equator (where cold spot identification is expected to be most accurate and complete) indicates the presence of significant clustering ($P = 0.99$ for a chi-square distribution using a complete spatial randomness test). Observational bias (due to the difficulty of identifying cold spots

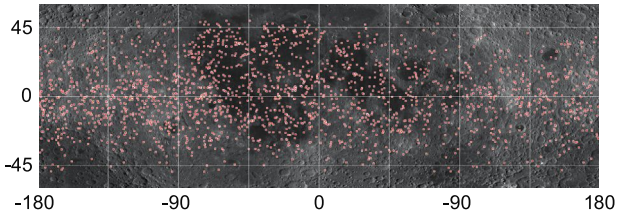

Fig. 1. LROC WAC global mosaic showing the locations of 2060 cold spots. Significant errors of omission are probable, especially at high latitudes.

in highlands terrains and especially at high latitudes) is likely to be one cause for this clustering, though it is unclear whether other factors are present. Assuming there is no latitudinal control on the distribution of cold spots and that the 693 cold spots identified between 10°S and 10°N is accurate, we estimate that the total number of cold spots across all lunar surfaces surfaces is close to 4000.

In addition, we selected 24 cold spots (Table 1) for more detailed and quantitative analysis using the Diviner rock-free regolith temperature data. The selection of these cold spots was based on their location within 10 of the equator in order to remove temperature variations based on latitude. They are also larger and more prominent than most cold spots, which allows for a greater number of temperature measurements. For comparison, we defined a background rock-free regolith night-time temperature curve using all Diviner data equatorward of 10°N/S. As stated above, both cold spots and warm, rocky crater surfaces cover only a small fraction of the surface and do not contribute significantly to the average regolith temperature (~0.1 K). These properties allow for the compilation of typical lunar regolith and cold spot diurnal temperatures. The rock-free regolith temperature data were averaged and placed in 15 min local time bins (Fig. 2).

The cold spot surfaces appear to gradually fade to the background regolith temperature with increasing distance from the source crater and it is impossible to define the edges or boundaries of cold spot surfaces. For our purposes, cold spot surfaces were defined as having a surface temperature at least 2 K less than the background rock-free regolith temperature at the local time of the observation. The 2 K difference identifies thermophysically distinct surfaces and is well above the 0.94 K standard deviation in rock-free regolith temperatures determined from individual observations using the noise characteristics of Diviner (Paige

Table 1
Locations of the 24 equatorial cold spots used for more detailed study. Data were not available to compute optical maturity parameter for the crater near 74°E, 0°N.

East longitude	North latitude	Crater diameter (km)	Cold spot area (km^2)	Average radial distance (km)	Maximum radial distance (km)	Optical maturity (OMAT)
−42.82	3.46	0.14	37	3	3	0.25
−33.20	3.01	0.16	24	3	4	0.26
−115.91	8.22	0.19	18	2	2	0.36
−15.13	−1.57	0.20	15	2	3	0.26
160.61	−5.32	0.21	156	7	7	0.33
−119.04	2.44	0.22	22	3	4	0.36
45.44	2.47	0.22	50	4	8	0.35
−124.29	−0.75	0.23	17	2	3	0.33
62.49	−5.36	0.23	28	3	3	0.34
135.30	7.72	0.24	81	5	9	0.35
−122.83	4.77	0.30	177	8	9	0.38
162.71	−4.25	0.32	82	5	5	0.41
74.32	0.43	0.36	81	5	8	
161.34	−9.08	0.38	307	10	16	0.35
−152.24	0.87	0.46	354	11	11	0.40
−118.45	7.15	0.48	873	17	17	0.39
−82.25	5.16	0.49	223	8	12	0.40
−114.84	0.50	0.53	383	11	18	0.39
−71.04	5.23	0.67	482	12	14	0.41
109.91	−6.74	1.02	2068	26	50	0.41
−125.97	5.79	1.23	6281	45	68	0.47
−50.47	−0.26	1.44	2789	30	47	0.45
90.76	−5.39	1.46	8546	52	126	0.36
151.68	−4.08	1.55	19,036	78	189	0.44

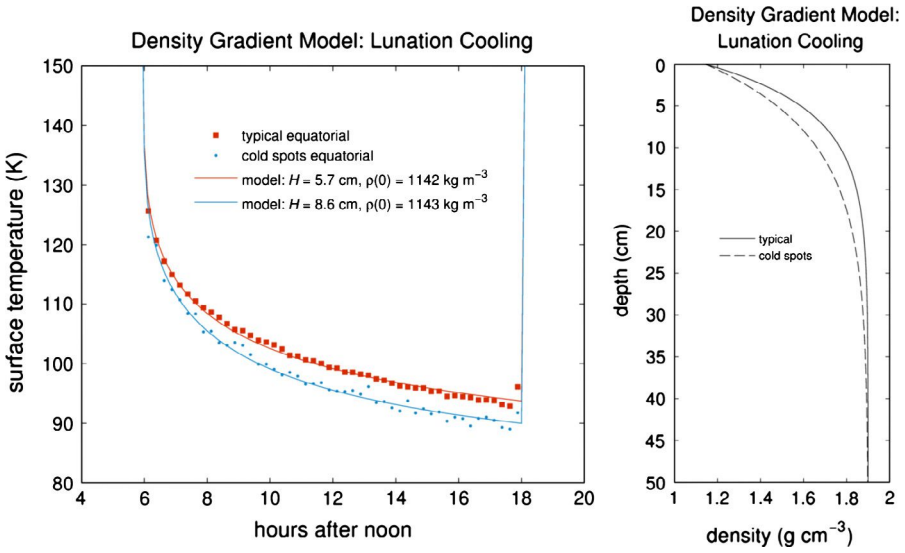

Fig. 2. Average night-time cold spot and background regolith measured (points) and modeled (lines) temperatures (left). Cold spot and typical regolith temperatures can be closely modeled assuming a regolith density that increases with depth. Cold spot regolith densities remain lower to greater depths than typical regolith surfaces.

et al., 2010). Total cold spot areas for each crater were calculated by summing the areas of each pixel in the 128 ppd images flagged with the 2 K difference.

We also identified areas of cold spot minimum temperatures surrounding each of the 24 craters examined in more detail in this study. The selection of these areas defines a diurnal night-time cooling curve where the thermophysically distinct surfaces within the cold spots are most prominent and temperature differences with the surrounding regolith surfaces are greatest. The minimum rock-free regolith temperatures for each of these areas were binned in 48 separate 15 min increments between 1800 and 0600 local times (Fig. 2). The resulting diurnal temperature variation is a compilation using data covering the 24 craters and does not represent the true diurnal temperature variation for any single surface. This compilation was necessary to build the full diurnal range of temperatures, which do not exist for any single cold spot surface. Although this temperature curve is derived from a number of locations, it displays a consistent temperature difference from the regolith background and may be used for the purpose of modeling the subsurface thermophysical properties and soil structure. These data define typical nighttime cold spot and surrounding regolith temperatures.

2.3. Thermophysical modeling

The lunar regolith has thermophysical properties consistent with variable density in the near-surface. This layering in typical lunar regolith was initially modeled as a 2 cm thick low density layer overlying higher density materials (e.g., Vasavada et al., 1999). With the increased precision and diurnal coverage of Diviner measurements, Vasavada et al. (2012) refined this model to show that a model of regolith density as an exponential function of depth produces model temperatures that more closely match measurements. This regolith density model follows the formula:

$$\rho_z = \rho_d - (\rho_d - \rho_0) \cdot e^{-(z/H)} \quad (1)$$

where ρ_z is the regolith density at depth z, ρ_0 is density at the surface, ρ_d is density at infinite depth, and H is the parameter that controls the e-folding density with respect to depth.

The average night-time equatorial cold spot and typical regolith night-time temperature curves were modeled with the H-parameter and ρ_0 (surface density) as free parameters (Fig. 2). We assumed a density of 1900 kg m^{-3} at infinite depth (Hayne et al., 2011). The detailed nature of the nighttime temperature curves allows for the modeling of both surface density and the H-parameter. We also derived the H-parameter for each pixel in the rock-free regolith temperature images. In this case, many pixels only had a single temperature measurement, making the derivation of more than one parameter non-unique. For the production of the H-parameter maps (Fig. 3), we assumed an exponential density profile, with fixed values of 900 kg m^{-3} at the surface (ρ_0) and 1900 kg m^{-3} at infinite depth (ρ_d; Vasavada et al., 2012; Hayne et al., 2011; Keihm and Langseth, 1973). The nighttime temperatures are most directly affected by the H-parameter and are relatively insensitive to the specific surface density value (ρ_0) used. To produce the H-parameter maps, we used a least-squares fit of the modeled surface temperatures to all available rock free regolith temperatures. Our finite-difference thermal model is similar to (and validated against) that of Vasavada et al. (2012), and incorporates a temperature- and density-dependent thermal conductivity (Hayne et al., 2011; Ghent et al., 2012). The exponential density profile produces a unique nighttime cooling profile that is subtly distinct from that produced by other regolith models. We also modeled the average regolith night-time temperatures using a simple two-layer model (Vasavada et al., 1999). In this case, modeled temperatures deviated significantly from measured temperatures (as discussed in detail by Vasavada et al., 2012).

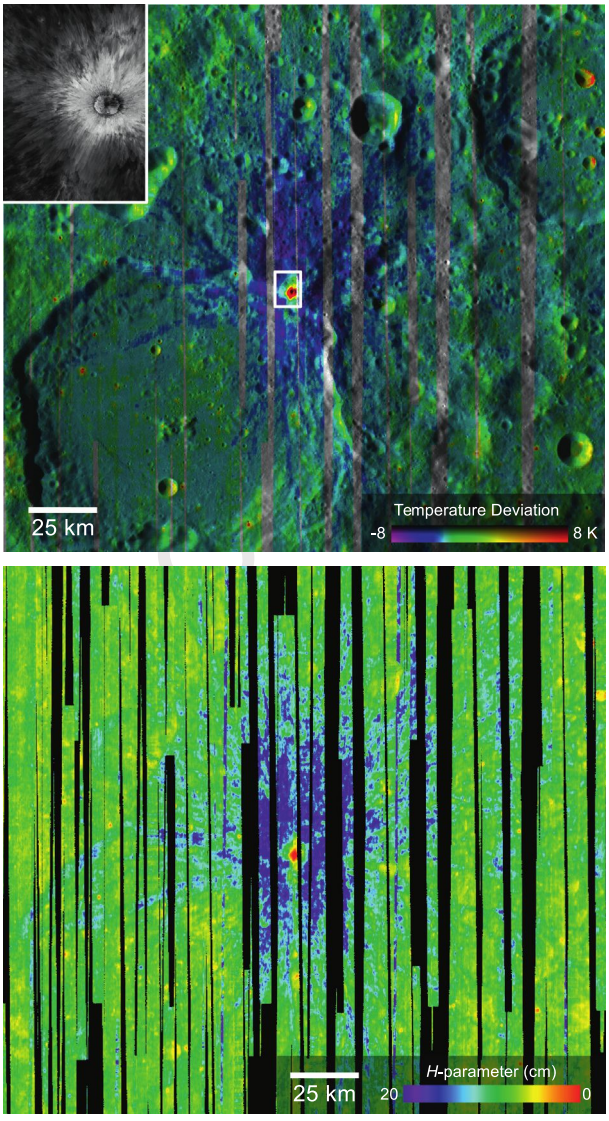

Fig. 3. (Top) Diviner night-time regolith temperatures relative to the global average showing a large cold spot surrounding a crater near 151.7°E, 4.1°S. Rocky surfaces close to the source crater have elevated temperatures (orange and red). The LROC WAC mosaic is used for shading. The white box denotes the area covered by the LROC image mosaic shown in Fig. 7 and the inset (upper left). (Bottom) H-parameter values for the large cold spot shown in the top image. Cold spot surfaces have a significantly thicker upper low density layer relative to typical lunar regolith. (For interpretation of the references to color in this figure legend, the reader is referred to the web version of this article.)

2.4. Optical maturity

To gain a sense of the exposure age of different surfaces, we calculated the optical maturity parameter (OMAT) following the methodology of Lucey et al. (2000a,b). Clementine near-infrared camera reflectance global mosaics at wavelengths centered at 0.75 and 0.95 μm are used to derive the OMAT parameter using the following equation:

$$\mathrm{OMAT} = [(R_{0.75} - x_0)^2 + ((R_{0.95}/R_{0.75}) - y_0)^2]^{1/2} \quad (2)$$

where R is the surface reflectance at 0.75 and 0.95 μm, x_0 is 0.08 and y_0 is 1.19. x_0 and y_0 are constants that represent values for a highly mature surface and are specific to the Clementine dataset. Less

mature surfaces have larger values of $R_{0.75}$ and $R_{0.95}/R_{0.75}$ and result in larger values of OMAT. This parameter accounts for both weakening of absorption band strength and lowering of albedo, which are both effects of space weathering processes and are more prominent for a surface that has been exposed for a longer period of time.

Non-cold spot fresh craters were selected for derivation of their OMAT values using latitude and size properties similar to those of the set of 24 cold spots examined in detail in this study (diameters of 0.14–1.54 km and within 10 degrees of the equator). In addition, the selected craters are not secondary in origin based on the radially symmetrical crater shape and (with one exception) ejecta pattern, lack of clustering with other fresh craters in the region, lack of association with crater chains, and the lack of an associated herringbone pattern (Oberbeck and Morrison, 1974). The selected craters are also not superimposed on rims or ejecta from larger fresh craters. The craters also have continuous relatively bright ejecta with both Diviner nighttime regolith temperature and Clementine multispectral data coverage to ensure adequate thermophysical and OMAT characterization.

3. Thermal properties

Cold spot surfaces have distinctive thermal properties. Each cold spot surrounds a fresh crater. Where the crater is large enough, the areas within and immediately surrounding the crater (typically within ~10 crater radii) have elevated temperatures (Fig. 3), consistent with the presence of boulders identified in high resolution images in and around these craters. The cold spot surfaces themselves have rock-free regolith temperatures up to 10 K cooler than the average surrounding regolith (Bandfield et al., 2011). Rock abundances are low (<0.5%) over cold spot surfaces (outside the proximal ejecta deposits) and Diviner brightness temperature data show temperature differences from the surrounding regolith that are similar to the more highly processed rock-free regolith temperatures. No cold surface anomalies of a similar magnitude were identified without a corresponding fresh crater near the center of the anomaly.

Cold spot daytime temperatures are not distinct from the surrounding terrain. The lunar regolith has low thermal inertia, both within and outside cold spots. This, combined with the relatively long diurnal cycle, results in daytime lunar surface temperatures that approach radiative equilibrium and are not significantly affected by subsurface thermophysical properties. In addition, as discussed in Section 5 (Visible Properties), cold spots have no distinguishing albedo features that would lead to daytime surface temperature differences.

The cool surfaces gradually approach the average surrounding regolith temperatures with increasing distance from the source crater. Rock-free regolith temperatures of cold spots and the surrounding terrain are initially similar prior to sunset, but typically diverge by about 5 K from average equatorial temperatures from sunset to 2100H local time (Fig. 2). This ~5 K difference is maintained throughout the lunar night.

The thermal cold spots have rayed profiles that mimic the visible proximal crater ejecta deposits. In most cases, these profiles are radially symmetrical, but there are occasional instances of lateral exclusion zones, indicating that a variety of impact angles may be represented (Fig. 4). Of the 24 craters listed in Table 1, only one shows evidence of exclusion zones in either the visible ejecta or cold spot.

Cold spots are present over a variety of surface types, including highlands, maria, dark mantled deposits, and radar dark halos (e.g., Ghent et al., 2005). Outside of cold spots, each of these terrains have remarkably similar nighttime regolith temperatures. Given the sensitivity of surface temperature to the fine scale structure of the lunar regolith, this indicates that the upper several 10s of cm of rock-free regolith in each of these regions has a similar structure and particle size. This is despite a clear contrast in the nature of the regolith at greater depths that shows considerable variability (e.g., Ghent et al., 2005; Bandfield et al., 2011). The presence of cold spots in each of these terrains also indicates that they are all modified in a similar manner by the cold spot formation process(es) and the source terrain has little effect on their formation.

4. Modeling and scaling relationships

As described above, cold spot surfaces are defined as having a temperature 2 K less that the average equatorial regolith temperature at the local time of the observation. Although somewhat arbitrary, this temperature difference reflects a significant physical difference in the upper several centimeters of the lunar regolith (e.g., Vasavada et al., 2012). Using this definition, we calculated total cold spot area and the maximum radial distance of a cold spot surface (termed maximum "runout distance" by Schultz, 1992) for each of the 24 equatorial cold spots listed in Table 1.

For these regions (with crater diameters of 140–1540 m) the average cold spot surfaces extend from 20 to 101 crater radii and the maximum radial distance for each crater extends from 25 to 244 crater radii (Fig. 5). The relationship between crater radius

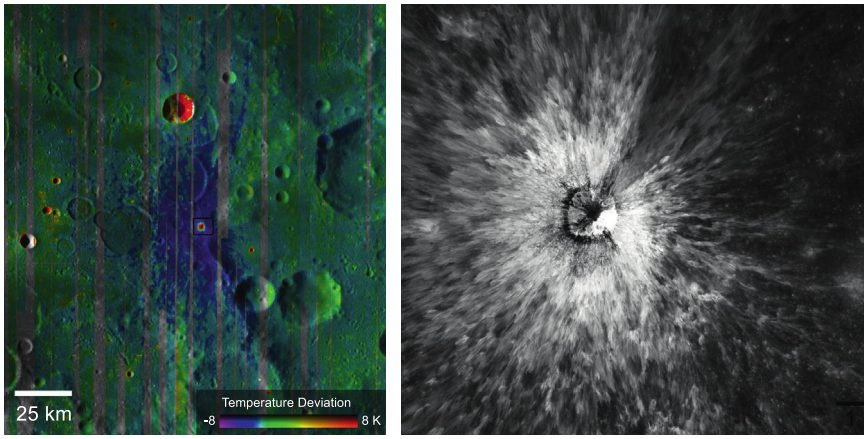

Fig. 4. (Left) Diviner night-time regolith temperatures relative to the global average showing a large cold spot surrounding a crater near 90.8°E, 5.4°S. The LROC WAC mosaic is used for shading. The small white box near the center of the image denotes the area covered by the LROC image in the right panel. (Right) LROC image mosaic (M185290442L/R; solar incidence 19°) showing proximal layered ejecta deposits. Both the proximal deposits and the cold spot are less prominent towards the east.

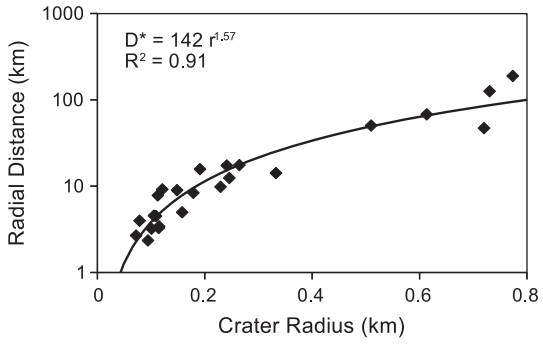

Fig. 5. Cold spot maximum radial distance versus crater radius. The regression (solid line) has a positive exponent and the high correlation coefficient shows that the data can be well modeled using a simple power function.

and maximum radial distance is fit well by an exponential regression with a correlation coefficient (R^2) of 0.91 (Fig. 5).

The maximum radial distance as a function of crater radius can be fit using a power function after the manner of Schultz (1992) and Ghent et al. (2010). Schultz (1992) found the exponent in this regression can be used to constrain the style of emplacement; a value of less than unity is indicative of ejecta constrained by an atmosphere, a value near unity is consistent with ballistic emplacement, and a value greater than unity may indicate emplacement by turbulent flow. For the 24 cold spots studied here, the exponent in the regression is 1.57 consistent with turbulent flow. A significant difference, however, is that our measurements apply to the cold spot surfaces, not the visible proximal ejecta (that lack evidence for turbulent flow) and it is not clear whether these scaling relationships can be connected to the formation process in the same manner.

The area of cold spot surfaces associated with each crater ranges from 37 to 19,037 km^2, although the largest cold spot is more than twice the area of the second largest (8546 km^2). Much smaller cold spots were identified and associated with craters as small as 60 m in diameter (Fig. 6). The total area for the 24 cold spots is 42,131 km^2, which is 0.64% of the lunar surface within 10 degrees of the equator. In addition to these 24 cold spots there are 669 additional cold spots that have been identified within 10 degrees of the equator (Fig. 1), where these features are most easily identified. Most of these cold spots are too small or faint to have a clearly defined surface area and are smaller than the 24 cold spots listed in Table 1. However, a rough estimate of an average area of 25 km^2 for each of the 669 cold spots makes up an additional 16,725 km^2 and 0.25% of the lunar surface within 10 degrees of the equator. These

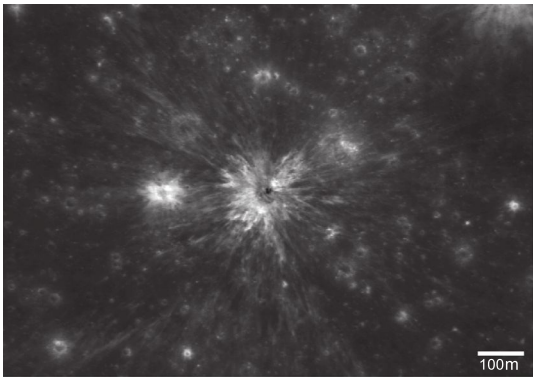

Fig. 6. LROC Narrow Angle Camera image (M185991440L) centered near 344.05°E, 17.56°N. The image shows a small ~60 m diameter crater that has thermophysical and morphological properties similar to other cold spot craters. Relatively cold nighttime surface temperatures extend across the entire surface shown.

estimates suggest that cold spots cover approximately 1% of the total lunar surface, regardless of terrain type.

The average nighttime temperatures for the 24 equatorial cold spots and the typical lunar regolith were fit assuming an exponential density profile using the H-parameter described in Section 2.3 (Fig. 2). Average cold spot night-time temperatures can be matched by H-values ~3 cm larger than typical regolith (8.6 versus 5.7 cm). The modeled surface density (ρ_0) is nearly identical between the cold spot surfaces and typical lunar regolith (1142 versus 1143 kg/m^3).

A distinguishing feature of cold spots is their persistence throughout the night, indicating that their anomalous thermophysical properties extend to at least several centimeters depth. The modeling shows that the only apparent difference between cold spot surfaces and the surrounding regolith is in the vertical distribution of materials. There is no indication that cold spot surfaces contain lower thermal inertia materials than the surrounding terrain. Low density materials are present near the surface for both surface types, but these low density materials extend to greater depths over cold spots relative to typical lunar surfaces.

We also tested the fit of cold spot and typical regolith nighttime temperatures using a simple 2-layer thermophysical model. The average cold spot cooling curve could be modeled by an upper low density layer ~2 cm thicker than typical lunar regolith, similar to the results using our density gradient model. However, as shown by Vasavada et al. (2012), the simple 2-layer model could not be used to match the measured temperatures as closely as the exponential density profile model. The cold spot temperatures clearly indicate the presence of low density materials that extend at least several centimeters deeper than typical regolith regardless of the details of the modeling. The nighttime temperatures are sensitive to both the thermal inertia of the surface materials and their thickness. For example, the substitution of a thinner, but lower thermal inertia layer for a thicker higher thermal inertia layer produces a surface that cools more quickly immediately after sunset, but more slowly later in the lunar night. This difference can be clearly distinguished in the diurnal temperature measurements. A more complete description of the sensitivity of surface temperatures to the model parameters is described in Vasavada et al. (2012).

The H-parameter was derived on a pixel-by-pixel basis using the Diviner rock-free regolith temperature maps. The H-parameter map of the cold spot shown in Fig. 3 (near 151.7°E, 4.1°S) indicates that the most prominent cold temperature anomalies have H-values of up to ~20 cm (Fig. 3). Although many cold spots surfaces show a distinction from surrounding terrain in the upper few centimeters of the lunar regolith, the most prominent cold spot surfaces show that the regolith has been modified to at least several 10s of cm depth.

Scaling relationships for lunar craters indicate that ejecta thickness diminishes with distance from the crater rim in a manner proportional to the crater radius cubed (McGetchin et al., 1973):

$$t(r) = t_0(r/R)^{-B} \quad (3)$$

where t_0 is the ejecta thickness at the crater rim, r is the distance from the crater rim, R is the radius of the crater, and B is a constant (~3.0 in a vacuum based on nuclear craters and large lunar craters; McGetchin et al., 1973). Under any reasonable assumption of the ejecta thickness at the crater rim, the thickness of the ejecta quickly diminishes and becomes insignificant with increasing distance from the crater. For example, the prominent cold spot located near 151.7°E, 4.1°S extends an average of 78 km from the 1.54 km diameter source crater. The crater ejecta thickness relationship described by Eq. (3) shows that even with a 20 m thick ejecta deposit at the crater rim, the ejecta thickness quickly drops to less than 1 cm within 10 km of the crater.

In order to affect surface temperatures throughout the lunar night, the disturbed regolith layer must be thicker than the thermal skin depth, about 3–5 cm for typical lunar surfaces assuming a thermal conductivity consistent with the results of Vasavada et al. (2012). Equating the thermal skin depth (3–5 cm) to the ejecta thickness ($t(r)$ in Eq. (3)) provides an estimate of the maximum distance from the crater rim where the ejecta should be apparent in the thermal data. For example, this cutoff is ~5–10 km for the 1.54 km diameter cold spot crater shown in Fig. 3. By comparison, the anomalously cold surfaces cover an area >19,000 km^2 with an average distance of 78 km from the source crater (Table 1). We also integrated cold spot H-values over their areas to derive a volume estimate for the material responsible for the thermal anomaly. Again, these values were several orders of magnitude larger than the volume of the excavated crater.

These relationships are only rough approximations. However, the data and modeling clearly show that cold spots are caused by a relatively thick layer of material over widespread areas. The thickness of this material is disproportionate to the volume of the source crater and ejecta scaling relationships and it is unlikely that the cold spots are dominated by ejecta from the crater itself.

5. Imaging and reflectance properties

5.1. Morphological properties

The terrain immediately surrounding craters associated with cold spots has distinct morphological and albedo features. In LROC NAC images, we observe two basic surface types; (1) bright layered surfaces close to the source crater that are not part of the cold spot temperature anomalies; and (2) the cold spot surfaces themselves, which appear to have been only subtly modified.

The proximal, radially-symmetric ejecta blankets (within ~5–10 crater radii) have a distinct layered appearance, with multiple overlapping lobes of radially striated material with abrupt snout-lobe-like terminations (Fig. 7). Material in the lower-most layers appears to have traveled the furthest. Successive superimposed layers terminate progressively closer to the source crater and are progressively lighter-toned. The radial striations wrap around obstacles, including some blocks that were present prior to deposition of the layers, but rarely coalesce downstream from obstacles; rather they continue in a linear fashion until their termination. Blocks >1 m across are visible and also litter the area on top of the layers immediately surrounding the source craters. Based on these observations, the deposition of the blocks occurred both prior to and after the emplacement of the proximal ejecta blankets.

High solar incidence angle images show that each layer can have significant topographic relief (Fig. 8), though this is not typically the case for cold spots associated with smaller craters. Lunar Orbiter Laser Altimeter (LOLA; Smith et al., 2010) elevation profiles (using elevation points from LRO orbit 1433) correlated with LROC images show topographic steps of up to 15 m between successive layers, though it is not clear if these thick layers are typical. The surfaces within the layers have a hummocky appearance, but it is unclear if this due to a draping of pre-existing surfaces or is a characteristic of the deposit itself. The cold spot surfaces and the proximal ejecta deposits appear to be mutually exclusive at the scale of the Diviner observations (~200–400 m/pixel) and the visible layered ejecta do not show anomalously cold temperatures. It is also not clear whether the warmer temperatures are due solely to the presence of rocks or if regolith layering is also a factor. The proximal deposits are covered by only a few Diviner pixels and both small and buried rocks can cause elevated rock-free regolith temperatures (Bandfield et al., 2011).

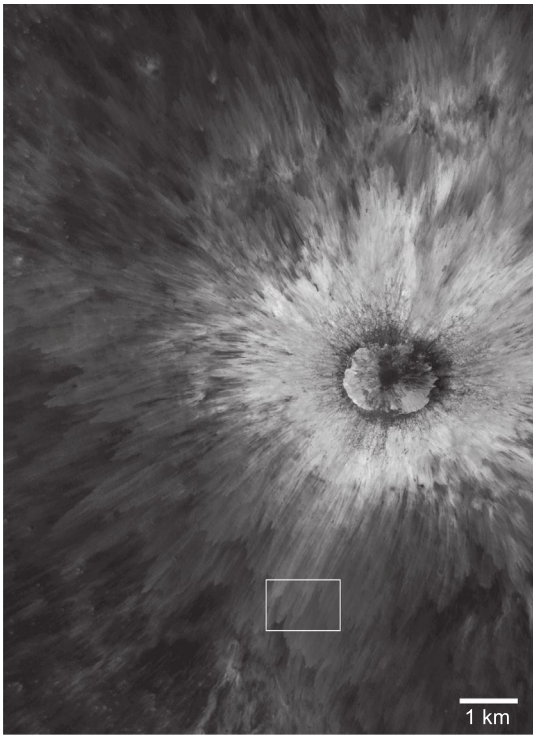

Fig. 7. Mosaic of LROC images M110601418L/R and M125936995L/R centered near 151.7°E, 4.1°S. This image shows the proximal layered ejecta deposits with their continuous, striated character. As shown in Fig. 3, cold spot surfaces are further away from the crater than these deposits. The white box denotes the area of detail shown in Fig. 3.

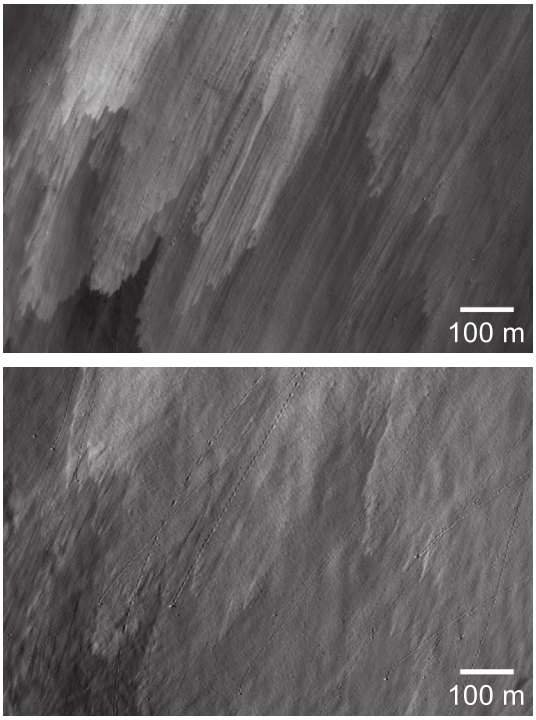

Fig. 8. LROC images M11060141R (top; solar incidence 17°) and M118858378R; solar incidence 66°). Both images cover the same location denoted by the white box shown in Fig. 7. High angles of solar incidence illustrate the surface textural characteristics and low angles of solar incidence show the albedo characteristics of the proximal layered ejecta deposits.

5.2. Optical properties

The optical maturity of the continuous ejecta immediately surrounding cold spot craters is distinct from that of non-cold spot craters (Fig. 9; Tables 1 and 2). Based on the optical maturity properties, cold spot craters appear younger than other non-cold spot bright, fresh craters. This may indicate that most small craters follow a similar development pattern but the distinct features associated with cold spots do not persist for long in the lunar environment. Consistent with this idea, we have identified several occurrences where the distinct layered proximal crater deposits are present but do not have an associated cold spot (Fig. 10). However, in these cases the deposits are more optically mature, the layering is not as distinct and there is a relatively large abundance of small craters on the ejecta. This indicates that the surface is older than the proximal crater deposits associated with cold spots. The apparently ephemeral nature of the cold spots is consistent with the relatively small thickness of cold spot surface materials (less than several 10s of cm) relative to the proximal deposits (greater than several meters thick).

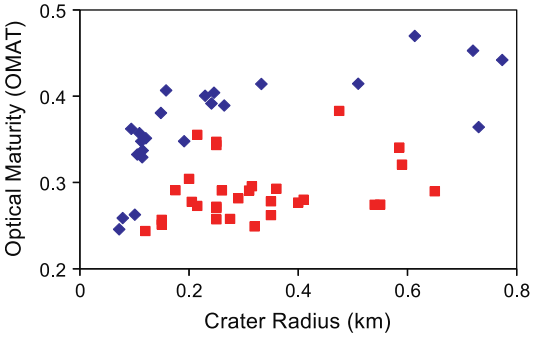

Fig. 9. Optical maturity parameter (OMAT) for near crater ejecta deposits that have surrounding cold spots (blue diamonds) and those that lack corresponding cold spots (red squares). Higher OMAT values indicate less mature surfaces. Cold spot crater ejecta (though not the cold spots themselves) are typically less mature than non-cold spot craters. Maturity values are lower for smaller craters due to incomplete blanketing of the surface and the limited resolution of the Clementine imaging data used for the calculation of the OMAT parameter. (For interpretation of the references to color in this figure legend, the reader is referred to the web version of this article.)

Table 2
Non-cold spot crater locations and maturity parameters.

E. longitude	N. Latitude	Crater diameter (km)	Optical maturity (OMAT)
97.33	−4.07	0.24	0.24
73.31	−2.33	0.30	0.25
21.88	5.68	0.30	0.26
9.60	5.22	0.35	0.29
108.47	−2.90	0.40	0.30
111.72	−4.35	0.41	0.28
25.45	3.53	0.43	0.27
−46.97	−9.08	0.43	0.36
62.00	0.78	0.50	0.26
45.31	−0.92	0.50	0.27
14.72	4.06	0.50	0.27
4.83	4.79	0.50	0.34
12.14	3.84	0.50	0.35
127.12	−7.66	0.52	0.29
97.39	−5.72	0.55	0.26
7.81	5.72	0.58	0.28
152.82	3.55	0.62	0.29
14.77	5.13	0.63	0.30
25.41	0.47	0.64	0.25
21.74	4.62	0.70	0.26
143.34	−5.23	0.70	0.28
149.93	0.58	0.72	0.29
35.30	0.47	0.80	0.28
49.41	−0.79	0.82	0.28
−151.76	2.10	0.95	0.38
−144.42	−0.68	1.08	0.27
138.66	−5.68	1.10	0.27
−112.98	−3.06	1.17	0.34
77.30	6.35	1.18	0.32
163.58	1.90	1.30	0.29

Fig. 10. LROC image (M140453816L) near 276.6°E, 13.2°N of a crater that lacks a surrounding cold spot. Although the proximal layered ejecta deposits are present, they are degraded and contain numerous small impact craters indicating their maturity relative to craters with surrounding cold spots (see Figs. 4 and 7 for comparison).

The cold spots are not detectable in reflected light datasets and show no distinguishing patterns in wide angle visible or near-infrared wavelength images with either high or low angles of solar incidence. Clementine UV/VIS/NIR albedos over cold spot surfaces (not including the proximal deposits) are variable, averaging 0.0031 (1–2% relative) higher within the 24 equatorial cold spots compared to the surrounding terrain. There is also no apparent spectral difference in Clementine reflectance data between the anomalously cold surfaces and the surrounding terrain. Calibrated LROC NAC albedo values were produced and compared with cold spot temperature anomalies (Fig. 11). Cold spot surfaces do not show systematic albedo or spectral trends that correlate with night-time surface temperatures.

There are subtle distinguishing features present within cold spot areas visible in high resolution LROC NAC images. Slightly brighter, "wispy" features with variable lengths and widths are sometimes present trailing away from the source crater behind topographic features (Fig. 12). Although these features are recognizable in high resolution images, they are limited in extent and surfaces that correlate with the strongest cold spot temperature anomalies appear featureless in the high resolution images.

6. Mechanism of formation

6.1. Surface properties

The layered nature of the deposits, deflection around obstacles, and the presence of flow lines strongly suggest transport and deposition by lateral flow for the proximal crater ejecta blanket.

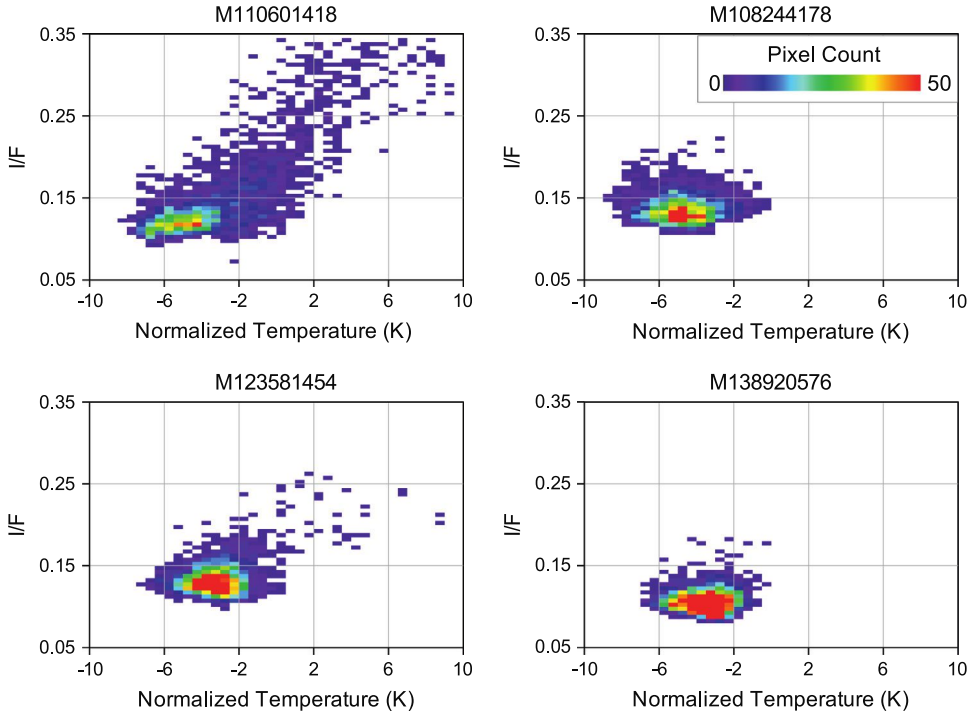

Fig. 11. Calibrated LROC Narrow Angle Camera *I*/*F* values versus Diviner nighttime regolith temperatures (relative to the global average). No clear trend is apparent between the surface reflectance and regolith temperature, with the exception of image M110601418 that includes relatively bright and warm, rocky ejecta deposits. All data were binned at 128 ppd.

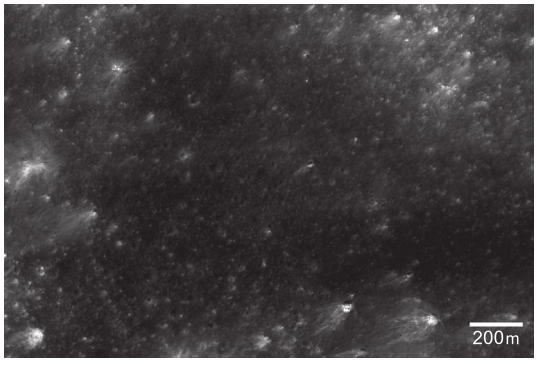

Fig. 12. LROC image (M123581454R; solar incidence 12°) covering a cold spot surface near 151.0°E, 4.2°S. Relatively bright, wispy surfaces trail away from the nearby source crater behind topographic features. However, the most prominent cold temperature anomalies coincide with relatively dark featureless surfaces within the image shown.

Although the proximal crater deposits have the appearance of discrete layers, it is not necessarily the case that they are generated via separate events. It is possible that the lateral flows progressively lose energy, terminating closer to the source, similar to progressive aggradation that causes a layered appearance in individual volcanic pyroclastic deposits on Earth (Branney and Kokelaar, 2002). Although progressive aggradation is common in flows, pulsating source conditions may also be responsible for the appearance of separate layers and cannot be entirely ruled out.

The striations and the abrupt termination-snouts resemble levees formed in many types of granular flow (e.g., Félix and Thomas, 2004). The lack of flow re-convergence downstream from obstacles and formation of levees strongly support transportation by granular flows in which transport is dominated by particle–particle interactions (dominantly frictional interaction with a minor influence of grain collisions) and cohesive forces between grains and gas–grain interaction is negligible (Branney and Kokelaar, 2002; Félix and Thomas, 2004). More turbulent flows strongly controlled by the presence of gases or suspension via grain collisions are not as laterally confined and would (for example) re-converge quickly after being diverted by obstacles (Félix and Thomas, 2004).

By contrast, we could only distinguish cold spot surfaces using nighttime thermal infrared measurements. They have no distinguishing albedo, spectral, or morphological characteristics. Cold spots have a similar optical maturity to the surrounding terrain, despite a young source crater with optically immature proximal ejecta. Although cold spots are apparently formed by impact events, their imaging properties show that they are composed of the same materials as the unmodified surrounding lunar regolith. The only modification to the cold spots surfaces that lie beyond the proximal layered apron appears to be a "fluffing-up" of the upper several centimeters of the surface without any deposition or stripping of material; either of which would modify the albedo and color of the surface. This material could not have been excavated from depth or sourced from the crater as either would expose relatively fresh, unweathered materials as well as higher inertia materials that would raise nighttime temperatures. In addition, as discussed in Section 4, the volume of cold spot material is too large to have come solely from the source crater.

6.2. Formation mechanisms

We have two hypotheses to explain the formation of the cold spots and the proximal layered deposits; (1) formation of both the proximal layered deposits and the cold spots via a cascading series of secondary impacts (similar to what has been termed ballistic erosion and sedimentation; Oberbeck, 1975); (2) proximal layered deposits formed as described in Hypothesis 1, but cold spot surfaces further from the source crater were formed by gas flows across the lunar surface.

Oberbeck (1975) and Oberbeck et al. (1975) describe dune-like morphologies associated with crater ejecta. Initially, dilute pyroclastic density currents (base surges) were invoked as an explanation for these deposits, but the difficulty of forming base surges in a vacuum environment led Oberbeck (1975) to put forth the hypothesis that was termed ballistic sedimentation. In this process, material is ejected with a high horizontal velocity. Upon impact of this material with the surface, this horizontal velocity is transferred to other materials that are then ejected (entrained) and also impact the surface, causing a cascading effect. This model has been subsequently tested and validated since its introduction (see Osinski et al., 2012 for a review). With the presence of solid rock surfaces, impact velocities need to be high enough to break apart and eject new materials. As a result this process was thought to be limited to larger craters than those shown here with high ejecta velocities.

In the case of cold spot craters, the surfaces affected are composed of loosely consolidated fine particulate regolith. Near the source crater, the high volumes of ejecta and their relatively large particle sizes may allow for the disruption of the surface layer to the point where enough material is dislodged to produce a laterally moving granular flow. Deposits would become darker and less weathered with increasing distance from the crater as a greater proportion of local weathered regolith is incorporated into the flows. In this manner, small craters can produce granular flows through the interaction of crater ejecta with the surrounding regolith.

Beyond the proximal layered deposits, the volume and size of the ejecta are too low to initiate flows or excavate material from beneath the weathered surface layer. However, the surface can still be disrupted by the impact of small grains that could disrupt the upper few to 10s of centimeters of material. Given the lack of evidence for deposits of ejecta within cold spot surfaces and the large distances from the source crater, impact velocities would need to be high enough to allow relatively small number of ejecta grains to disrupt a large amount of regolith.

This formation mechanism implies that there is a point at which enough material is disrupted to initiate granular flow. This is similar to the ballistic sedimentation mechanism of Oberbeck et al. (1975) but appears to be associated with much smaller craters than initially proposed. The boundary between the proximal layered deposits and the cold spot surfaces appears to bridge this transition point. The impact of individual particles on the surface results in effective lateral and vertical mixing of materials. By contrast, granular flows cause high amounts of shear stress that effectively "smears" materials laterally with minimal vertical disruption. Traces of these granular flow deposits should be common in the lunar regolith.

A perplexing aspect of the cold spot surfaces is that significant areas have been subtly modified without the addition or stripping away of significant material. Our hypothesis that these surfaces are disrupted by solid ejecta from the source crater relies on a balance of several factors. These include minimal emplacement of new material, minimal excavation to a depth that would expose unweathered material, and relatively continuous disruption of the upper several cm of the surface across broad areas. It is not clear if this precise set of conditions can be commonly met for typical lunar impacts.

Alternately, the cold spot features may be formed by a lateral flow of gas across the lunar surface. The gas could be derived from either the impactor or target and driven by the energy of the impact. The presence of a gas would be gravitationally bound, but with high mobility that would explain the extremely large maximum radial distances associated with the cold spots. The initial arrival of the gas at a surface may result in an overpressure, similar to nuclear explosions or volcanic gas flows (Glasstone and Dolan, 1977; Valentine, 1998). In fluidized flows an underpressure develops as the flow head passes over the surface, creating lifting and shearing forces that may be capable of disrupting and decompressing the upper several centimeters of the surface (Roche et al., 2012). The presence of a gas flow allows for relatively gentle modification of large areas relative to crater size without the deposition of new material.

Both of these hypotheses appear to be feasible based on qualitative relationships. However, they also require a more quantitative assessment using models and laboratory experiments that are beyond the scope of our primary goal here of documenting and interpreting the spacecraft measurements. Regardless, it is clear from the observations that processes in addition to simple ballistic emplacement of ejecta modify extensive surfaces surrounding small lunar craters.

An alternate formation mechanism could be linked to seismic events associated with the impact. However, seismic intensities do not form rayed patterns radially symmetrical about the source (e.g., Sadigh et al., 1997). The rayed nature of the cold spots and their radial similarity to the proximal ejecta imply an external and/or surface process and preclude seismic effects of the impact as the sole formation mechanism.

6.3. Implications for lunar regolith development

The lunar regolith is delicately structured and even minor changes cause significant differences in the thermophysical properties and resulting surface temperatures. This delicate structure combined with the relative quiet of the lunar surface environment preserves otherwise ephemeral features that would be quickly erased (and may not have formed to begin with) on planets with active aeolian and fluvial processes such as Earth or Mars. Indeed, we found no instances on Mars of the unique morphological and thermophysical properties associated with the cold spot craters discussed here. The cold spot crater properties described here appear to be common to all craters in the lunar environment but are degraded over time, leaving only more durable and large scale features.

We can estimate the frequency by which lunar surfaces are modified by the cold spot formation process. Assuming a 0.2 km diameter crater with a $\sim$50 km^2 associated cold spot and an impact rate of $\sim 1 \times 10^{-9}$ km^{-2} yr^{-1} (Le Feuvre and Wieczorek, 2011), any surface is likely to be affected about once every 20 myr. Approximately 1% of the lunar surface is currently covered by cold spots. Using the cratering rate listed above and assuming that all impacts result initially in a cold spot surface, our results suggest that cold spot features must not persist longer than several hundred thousand years.

The cold spots cover vast areas relative to the source crater size and the influence of small impacts on the lunar surface may be much greater than previously recognized. However, the lack of exposed immature surfaces indicates that this influence is limited to the upper 10s of cm based on the thickness of the homogenized upper mature layer identified in Apollo core samples (e.g., Heiken et al., 1991). Regardless of the formation mechanism, small impacts may be responsible for overturning and homogenizing the upper few cm to 10s of cm of regolith throughout lunar history. Micro-sized impacts also likely play a role in the churning of the upper lunar regolith, but perhaps at a more constant rate and on a much smaller scale.

The proximal layered deposits indicate that most ejecta are emplaced via granular flow and flow features appear to be common to all small lunar craters. Although the proximal crater deposits do not cover nearly as large an area, they also have a significant influence on the structure of the lunar regolith. Layered sequences are likely to be common within the lunar regolith and the constant

interaction with the surface materials via lateral flow allows for greater incorporation of these materials in the ejecta deposits.

These features should be present on any low thermal inertia airless body with significant gravity and we would expect them to be detected on other Solar System objects when high resolution thermal and visible wavelength observations become available. Unfortunately, the Dawn and Mercury Surface, Space Environment, Geochemistry, and Ranging (MESSENGER) spacecraft have not imaged the surfaces of Vesta or Mercury at high enough resolution to detect similar proximal layered deposits. In addition, neither spacecraft is able to acquire nighttime temperature measurements that would allow for the detection of features similar to the cold spots.

7. Conclusions

Detailed morphological and thermophysical measurements of the lunar surface show that cratering in the vacuum environment involves a previously unrecognized set of processes that leave prominent, but ephemeral, features on the lunar surface. It appears that granular flow may be a common and even the dominant mechanism of ejecta emplacement from small impact events. These flows may be formed through a cascading effect of crater ejecta dislodging and incorporating near surface loose regolith materials that result in a lateral flow across the surface.

Beyond the granular flow features are extensive regions of low density and highly insulating surface materials formed by small impacts. These surfaces are formed through the disruption of the upper few to 10s of centimeters of regolith without excavating or depositing significant amounts of new material. We are uncertain of the mechanism involved, but we put forth two hypotheses that invoke small secondary impacts or mobilized gases to disrupt the near surface.

The cold spot and granular flow features appear to be common to all small lunar impacts and may be present on other airless bodies. The great extent of the cold spot features relative to the crater size indicates that this is a process common to most lunar surfaces and is fundamental to the development of the structure of the lunar regolith.

Acknowledgments

We would like to thank the LRO, LROC, LOLA, and Diviner operations teams for the collection of high quality datasets used in this work. JMARS GIS software developed at Arizona State University was used for data analysis and production of several manuscript figures presented here. Discussions with Carl Allen, Ben Greenhagen, Hugh Kieffer, Noah Petro, Mark Robinson, and Pete Schultz helped us make what we hope is better sense of the cold spot features. Robin Fergason and Gordon Osinski provided detailed formal reviews that significantly improved the clarity and content of this manuscript.

References

Bandfield, J.L. et al., 2011. Lunar surface rock abundance and regolith fines temperatures derived from LRO Diviner Radiometer data. J. Geophys. Res., 116. http://dx.doi.org/10.1029/2011JE003866.

Boyd, A.K., Robinson, M.S., Sato, H., 2012. Lunar Reconnaissance Orbiter wide angle camera photometry: An empirical solution. Lunar Planet. Sci. 43. Abstract 2795.

Branney, M.J., Kokelaar, P., 2002. Pyroclastic Density Currents and the Sedimentation of Ignimbrites. Geological Society, London. Memoirs, 27.

Braslau, D., 1970. Partitioning of energy in hypervelocity impact against loose sand targets. J. Geophys. Res. 75, 3987–3999. http://dx.doi.org/10.1029/JB075i020p03987.

Félix, G., Thomas, N., 2004. Relation between dry granular flow regimes and morphology of deposits: Formation of levees in pyroclastic deposits. Earth Planet. Sci. Lett. 221, 197–213. http://dx.doi.org/10.1016/S0012-821X(04)00111-6.

Ghent, R.R., Leverington, D.W., Campbell, B.A., Hawke, B.R., Campbell, D.B., 2005. Earth-based observations of radar-dark crater haloes on the Moon: Implications for regolith properties. J. Geophys. Res., 110. http://dx.doi.org/10.1029/2004JE002366.

Ghent, R.R. et al., 2010. Generation and emplacement of fine-grained ejecta in planetary impacts. Icarus 209, 818–835. http://dx.doi.org/10.1016/j.icarus.2010.05.005.

Ghent, R.R. et al., 2012. Constraints on the recent rate of lunar regolith accumulation from Diviner observations. American Geophysical Union (Fall). Abstract 2012AGUFM.P42A07H.

Glasstone, S., Dolan, P.J., 1977. The Effects of Nuclear Weapons, third ed. U.S. Government Printing Office, Washington, DC.

Hayne, P.O. et al., 2011. The Moon's extremely insulating near-surface: Diviner infrared observations of a total lunar eclipse. American Geophysical Union (Fall). Abstract 2011AGUFM.P13D1712H.

Heiken, G.H., Vaniman, D.T., French, B.M., 1991. Lunar Sourcebook – A User's Guide to the Moon. Cambridge University Press, Cambridge, England, 753p.

Horai, K.-I., Simmons, G., 1972. Thermal property measurements on lunar material returned by Apollo 11 and 12 missions. Prog. Astronaut. Aeronaut. 28, 243–267.

Housen, K.R., Holsapple, K.A., 2011. Ejecta from impact craters. Icarus, 211. http://dx.doi.org/10.1016/j.icarus.2010.09.017.

Keihm, S.J., Langseth Jr., M.G., 1973. Surface brightness temperatures at the Apollo 17 heat flow site: Thermal conductivity of the upper 15 cm of regolith. Lunar Planet. Sci. 4. Abstract 2503.

Le Feuvre, M., Wieczorek, M.A., 2011. Nonuniform cratering of the Moon and a revised crater chronology of the inner Solar System. Icarus, 214. http://dx.doi.org/10.1016/j.icarus.2011.03.010.

Lucey, P.G., Blewett, D.T., Taylor, G.J., Hawke, B.R., 2000a. Imaging of lunar surface maturity. J. Geophys. Res. 105, 20377–20386. http://dx.doi.org/10.1029/1999JE001110.

Lucey, P.G., Blewett, D.T., Taylor, G.J., Hawke, B.R., 2000b. Imaging of lunar surface maturity. J. Geophys. Res., 105. http://dx.doi.org/10.1029/1999JE001110.

McGetchin, T.R., Settle, M., Head, J.W., 1973. Radial thickness variation in impact crater ejecta: Implications for lunar basin deposits. Earth Planet. Sci. Lett. 20, 226–236. http://dx.doi.org/10.1016/0012-821X(73)90162-3.

Melosh, H.J., 1989. Impact Cratering: A Geologic Process. Oxford University Press, New York, 253p.

Oberbeck, V.R., 1975. The role of ballistic erosion and sedimentation in lunar stratigraphy. Rev. Geophys. Space Phys. 13, 337–362. http://dx.doi.org/10.1029/RG013i002p00337.

Oberbeck, V.R., Morrison, R.H., 1974. Laboratory simulation of the herringbone pattern associated with lunar secondary crater chains. Moon 9, 415–2455. http://dx.doi.org/10.1007/BF00562581.

Oberbeck, V.R., Morrison, R.H., Hoerz, F., 1975. Transport and emplacement of crater and basin deposits. Moon 13, 9–26. http://dx.doi.org/10.1007/BF00567505.

Osinski, G.O., Tornabene, L.L., Grieve, R.A.F., 2011. Impact ejecta emplacement on terrestrial planets. Earth Planet. Sci. Lett., 310. http://dx.doi.org/10.1016/j.epsl.2011.08.012.

Paige, D.A. et al., 2010. The Lunar Reconnaissance Orbiter Diviner Lunar Radiometer Experiment. Space Sci. Rev. 150, 125–160. http://dx.doi.org/10.1007/s11214-009-9529-2.

Paige, D.A., Williams, J.P., Sullivan, M.T., Greenhagen, B.T., 2011. LRO Diviner Lunar Radiometer global mapping results and gridded data product. Lunar Planet. Sci. 42. Abstract 2544.

Roche, O., Nino, Y., Mangeney, A., Brand, B.D., Valentine, G.A., 2012. Entrainment of granular substrate by pyroclastic flows: An experimental study and its implications for flow dynamics. American Geophysical Union (Fall). Abstract 2012AGUFM.V52C07.

Sadigh, K., Chang, C.-Y., Egan, J.A., Makdisi, F., Youngs, R.R., 1997. Attenuation relationships for shallow crustal earthquakes based on California strong motion data. Seis. Res. Lett. 68, 180–189. http://dx.doi.org/10.1785/gssrl.68.1.180.

Schultz, P.H., 1992. Atmospheric effects on ejecta emplacement and crater formation on Venus from Magellan. J. Geophys. Res. 97, 6183.

Smith, D.E. et al., 2010. The Lunar Orbiter Laser Altimeter investigation on the Lunar Reconnaissance Orbiter mission. Space Sci. Rev. 150, 209–241. http://dx.doi.org/10.1007/s11214-009-9512-y.

Stopar, J.D., Robinson, M., Barnouin, O.S., Tran, T., 2010. Depths, diameters, and profiles of small lunar craters from LROC NAC stereo images. American Geophysical Union (Fall). Abstract 1543.

Valentine, G.A., 1998. Damage to structures by pyroclastic flows and surges, inferred from nuclear weapons tests. J. Volcan. Geotherm. Res. 87, 117–140.

Vasavada, A.R., Paige, D.A., Wood, S.E., 1999. Near-surface temperatures on Mercury and the Moon and the stability of polar ice deposits. Icarus 141, 179–193. http://dx.doi.org/10.1006/icar.1999.6175.

Vasavada, A.R. et al., 2012. Lunar equatorial surface temperatures and regolith properties from the Diviner Lunar Radiometer Experiment. J. Geophys. Res., 117. http://dx.doi.org/10.1029/2011JE003987.